




First Principles Investigations of Structural, Electronic and Transport Properties of $\text{BiI}_3/\text{ZrS}_2$ van der Waals Heterostructure: A Thermoelectric Perspective

GAUTAM SHARMA,¹ SHOUVIK DATTA,^{1,2}
and PRASENJIT GHOSH ^{1,2,3,4}

1.—Department of Physics, Indian Institute of Science Education and Research, Pune, Maharashtra 411008, India. 2.—Centre for Energy Sciences, Indian Institute of Science Education and Research, Pune, Maharashtra 411008, India. 3.—e-mail: prasenjit.jnc@gmail.com. 4.—e-mail: pghosh@iiserpune.ac.in

Using density functional theory and semi-classical Boltzmann transport theory, we have studied structural, electronic and transport properties of a van der Waals vertical heterostructure of BiI_3 and ZrS_2 . The elastic constant of the heterostructure is larger than the individual monolayers. Further it has a direct band gap that is smaller than the monolayers. The interaction between the layers results in subtle changes in the electronic properties of the heterostructure such that its transport properties are also affected. In particular, we find that the relaxation time of electrons is significantly increased in the heterostructure such that its power factor is about ten and one hundred times larger than that of a monolayer of ZrS_2 and BiI_3 , respectively, indicating that the maximum power output from a thermoelectric device made of an *n*-doped heterostructure is larger than that obtained from the individual components. Our results suggest that this novel heterostructure is a possible candidate for *n*-type thermoelectrics.

Key words: Thermoelectric, heterostructure, monolayer, power factor, ZrS_2 , BiI_3

INTRODUCTION

With the decline in availability of fossil fuels and increase in environmental pollution caused by their use as a primary source of energy, there is a tremendous growth in research activities related to developing alternative technologies that can harness renewable sources of energy. Additionally, much energy is also wasted in the form of heat. Hence, there are significant research efforts to develop technologies that can use wasted heat energy and convert it into some other useful form. Amongst them, thermoelectric (TE) materials have attracted particular attention because of their thermoelectric effects, e.g. the Seebeck effect can be

used to transform waste heat produced from industry, automobile engines, microprocessors, mobile phones, etc., directly into electrical energy.^{1,2} The efficiency of a TE material is determined by a dimensionless figure of merit, $ZT = \alpha^2 \sigma T / \kappa$, where α denotes the Seebeck coefficient, σ the electrical conductivity, T the absolute temperature and κ the total thermal conductivity, which is the sum of the contributions from the carrier (κ_e) and lattice (κ_L) thermal conductivities.³ The higher the value of ZT for a TE material, the better will be its performance. Amongst the above mentioned material parameters, α , σ and κ_e have complex interrelationships. For example, upon increasing the doping concentration σ increases while α decreases. Further, for a high value of ZT a material should have high electrical conductivity and low thermal conductivity. However, typically, materials with high electrical conductivity also have a high value of electronic

(Received June 12, 2020; accepted September 9, 2020; published online October 8, 2020)

thermal conductivity. All these factors make it immensely difficult to control the different material parameters independently to optimize ZT .

Based on theoretical calculations, Dresselhaus et al. predicted that reducing the dimensionality can significantly enhance the power factor and thereby ZT compared to their bulk counterparts.^{4,5} Following their predictions, researchers have developed novel routes such as nanostructuring^{6–11} and band structure engineering¹² to enhance the power factor. This has led to a large family of thermoelectric materials based on metal chalcogenides (Bi₂Te₃, Sb₂Te₃ and PbTe), superionic conductors, metal oxides, SiGe alloys, etc.³ Additionally, with the advancement in nanotechnology, several low-dimensional materials apart from graphene are being prepared with improved and/or novel properties. Amongst them phosphorene¹³ and transition metal dichalcogenides (TMDC)^{14–17} have been predicted to be possible candidates for thermoelectric applications. In a recent work, Lv et al. predicted that the ZrS₂ monolayer, which belongs to the family of TMDC and has a low lattice thermal conductivity, shows a high ZT value.¹⁸ They further showed that the Seebeck coefficient can be increased by engineering the band structure through strain, which results in an increased value of ZT .

In addition to TMDCs, there has been a relatively new family of materials with a chemical formula of MX₃, where X is a halide ion and M is a metal atom. Recently, there has been great interest in investigating its physical properties.^{19–23} Recent calculations by Liu et al. on MX₃ (where M=Sc, Y, As, Sb, and Bi) showed that these are semiconductors.²³ Amongst them, BiI₃ is particularly interesting because of the presence of a Mexican hat-like band structure in the valence band that might lead to a high value of Seebeck coefficient.²⁴ Moreover, it has been predicted that BiI₃ has a very low value of thermal conductivity.²⁵ However, it has a large value of effective masses for holes and a band gap that is larger compared to other semiconductors that are typically used for TE devices. These two properties might be detrimental for their performance as a thermoelectric device.

One way to improve material properties is to form van der Waals heterostructures. There have been many reports of such heterostructures (HS) that show enhanced transport properties. For example, Mohanta et al. showed that forming vertical heterostructures of boron monosulphide with MoS₂ show an enhanced value of ZT .²⁶ Nguyen et al.²⁷ showed that vertical HS of graphene layers show a larger value of ZT due to reduced thermal conductivity. In addition to vertical HS there are also efforts to form lateral HS of layered materials to improve ZT . For example Ding et al.²⁸ produces a two-dimensional superlattice-monolayer structure of ZrSe₂/HfSe₂ with a highly degenerate conduction level, which gives a high n-type power factor.

Based on the encouraging results reported in the previous studies, in this work, we have studied the structural, electronic and transport properties of vertical HS of ZrS₂/BiI₃. Besides the interesting properties of each individual component mentioned in the previous paragraphs, we also note that the lattice parameters of BiI₃ monolayer is twice that of ZrS₂. Hence, a (2 × 2) supercell of ZrS₂ is perfectly lattice-matched with that of a (1 × 1) supercell of BiI₃. Moreover, based on the positions of the valence and conduction band edges of the individual components, as reported in the literature,^{18,22} we show that the HS will most probably form a Type-II heterojunction, thereby having a smaller band gap compared to the parent components. This suggests that it may be interesting to investigate the properties of the HS for thermoelectric applications. The rest of the paper is as follows: Sect. [Computational Details](#) contains the computational details. The results are presented in Sect. [Results](#). Finally, we conclude in Sect. [Conclusion](#).

COMPUTATIONAL DETAILS

The calculations in the present work are performed using the Quantum ESPRESSO software, which is a plane wave-based implementation of density functional theory.^{29,30} The electronic exchange and correlation potential was described by the generalized gradient approximation (GGA) as parametrized by Perdew, Burke and Ernzerhof (PBE).³¹ We used ultrasoft pseudopotentials to account for the electron-ion interactions.³² The pseudopotentials were generated using $4s^2 4p^6 4d^2 5s^2$, $2p^6 3s^2 3p^4$, $4d^{10} 5s^2 5p^5$ and $4f^{14} 5d^{10} 6s^2 6p^2$ valence configurations for Zr, S, I and Bi, respectively. The kinetic energy cutoffs for the wavefunction and charge density used for the calculation are 80 Ry and 800 Ry, respectively. To sample the Brillouin zone (BZ), we used a (9 × 9 × 1) Monkhorst-Pack k-mesh.³³

Since we are using periodic boundary conditions, to avoid erroneous interactions between the periodic images we used 22 Å vacuum along the direction perpendicular to the plane of the monolayers and the heterostructure (z-axis of the unit cell in this case).

Earlier studies have shown that van der Waals interactions are important for these systems.²² However, these are not accounted for within the PBE exchange correlation functional. Hence, we used the semi-empirical Grimme-D2 van der Waals (vdW) corrections in all the calculations.³⁴ The vdW radius and the C_6 coefficients used in our calculations for each of the atomic species are listed in Table I. Additionally, since Bi and I are heavy atoms, spin orbit interactions (SOI) are important. To correctly account for the SOI, the Kohn-Sham equations were solved self-consistently using fully relativistic ultrasoft pseudopotentials.^{35,36} Further, standard PBE functionals are also known to severely underestimate the band gap. Since we are

Table I. van der Waals radius (r_{vdW}) and the C_6 coefficients for the different atomic species used in the Grimme-D2 vdW corrections. These values are taken from Ref. 34

Atomic species	r_{vdW} (bohr)	C_6 (Ry/bohr ⁶)
Bi	3.586	2204.274
I	3.575	1092.775
Zr	3.097	855.833
S	3.180	193.230

interested in transport properties of these materials and the latter in turn depends on the band gap, it is important to compute the band gap with reasonable accuracy. For that purpose the band structures for the monolayers and heterostructures were computed using the singularity-free Gaussian-attenuated Perdew-Burke-Ernzerhof (Gau-PBE) hybrid functionals.³⁷ To include the SOC effects along with the hybrid functional calculations, we used norm-conserving pseudopotentials with a plane wave cut-off of 125 Ry for Gau-PBE calculations.³⁸ The matrix elements of the Fock operator were evaluated with a $3 \times 3 \times 1$ q-mesh.

For transport property calculations, we used the BoltzTraP package,³⁹ which solves the semi-classical Boltzmann transport equation (BTE) within the constant relaxation time (CRT) and rigid band (RB) approximations.³⁹ While within the CRT approximation it is assumed that the relaxation time (τ) is same for all the electronic states, RB approximation considers that doping the material does not alter band dispersion and only results in a shift of the chemical potential of the system. For transport properties, we used $(57 \times 57 \times 1)$ k-point grid to obtain the Kohn-Sham eigenvalues, which are further fed into BoltzTraP code to yield transport properties.

Computation of τ : In addition to the CRT approximation, the Boltztrap code computes the transport properties in terms of τ . Hence, to know absolute values of the transport coefficients, we must compute τ . τ depends on several factors such as electron-phonon coupling, scattering by defects, and disorders. However, computing these from first principles is either difficult or for some cases impossible. The contribution to τ from electron-phonon coupling can be obtained from first-principles calculations. However, for our case, particularly for the HS, the unit cell is quite large. This, coupled with the fact that we must include SOC, made direct computation of τ impossible with our limited computational resources. Hence, in this work, we used the deformation potential theory, together with the effective mass approximation to obtain the phonon-limited mobility μ_{2D} from which we computed τ using the following equation:

$$\mu_{2D} = \frac{e\tau}{m^*} \quad (1)$$

where e is the charge of an electron and m^* is the effective mass of an electron. μ_{2D} is given by:

$$\mu_{2D} = \frac{e\hbar^3 C}{k_B T m^* m_d E_{dp}^2} \quad (2)$$

where C is the 2D elastic constant, $m_d = \sqrt{m_x^* m_y^*}$ is the average effective mass. $C = \frac{\partial^2 E}{\partial \delta^2} \frac{1}{A_0}$ is the elastic modulus of the 2D material. A_0 is the area of the surface unit cell. To compute C we applied uniaxial strain (δ) along the a direction and computed the total energy E of the strained system. From this we computed the second derivative of total energy with respect to strain at $\delta = 0$. The deformation potential (E_{dp}) is given by $E_{dp} = \partial E_{edge} / \partial \delta$, where E_{edge} is the edge of the valence and conduction band. In order to compute E_{dp} we computed the band structure of the system both under compressive and tensile strain. From the band structure we plotted E_{edge} as a function of strain. The plot is fitted to an equation of a straight line, the slope of which gives the value of E_{dp} . Therefore, from Eqs. 1 and 2 we get:

$$\tau = \frac{\hbar^3 C}{k_B T m_d E_{dp}^2} \quad (3)$$

RESULTS

Structure and Energetics

In bulk, both ZrS₂ and BiI₃ form layered structures, which are held together through weak van der Waals (vdW) interaction. Each layer of ZrS₂ (BiI₃) comprises three atomic layers where the atomic layer contains metal atoms, i.e. Zr (Bi) is sandwiched between two atomic layers of S (I). The three atomic layers (S-Zr-S of ZrS₂ and I-Bi-I of BiI₃) are stacked in an ABC pattern such that each of the metal cations are at the centre of the octahedron formed by the anions. Though both bulk ZrS₂ and BiI₃ belong to the hexagonal crystal system, their space groups are different. While the former has a P $\bar{3}m1$ space group, the latter belongs to the R $\bar{3}$ space group. A monolayer of these materials forms a two-dimensional hexagonal unit cell (Fig. 1). Our calculations at the level of PBE+vdW+SOC yield lattice parameters of 3.64 Å for a monolayer of ZrS₂ (ML-ZrS₂) and 7.41 Å for a monolayer of BiI₃ (ML-BiI₃). We note that these are in excellent agreement with previous literature reports.^{18,22,40} The Zr-S (Bi-I) bond lengths are 2.56 Å (3.11 Å). Further, the thickness of each ML, calculated by measuring the distance between the two anionic layers along the z -direction, is about 2.94 Å and 3.62 Å for ZrS₂ and BiI₃ respectively.

In order to make the vertical heterostructure (HS), i.e., where one layer is stacked over another, we begin by noting that the (2×2) 2D unit cell of ZrS₂ is almost lattice matched with the (1×1) unit

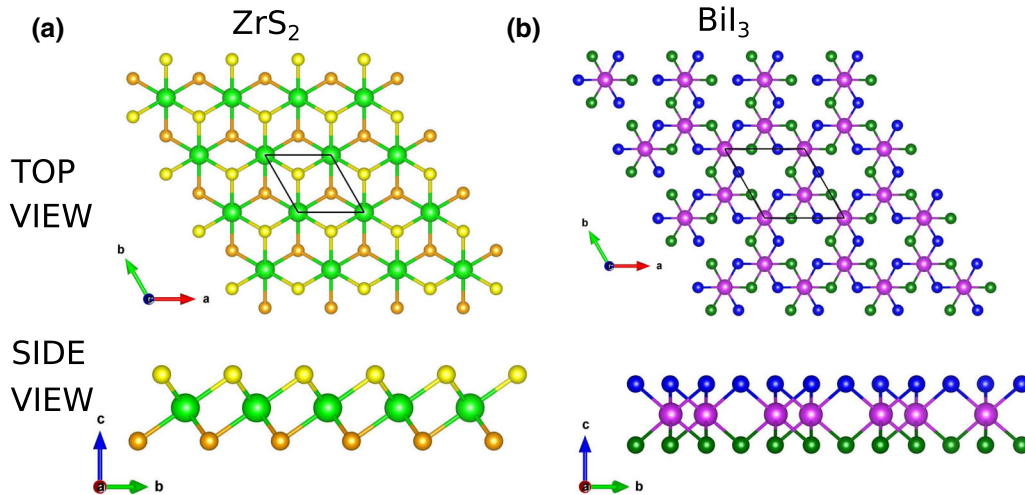


Fig. 1. The top and side views of the structures of a monolayer of (a) ZrS₂ and (b) BiI₃. The two-dimensional unit cell for each case is denoted by a black parallelogram. The large light green and violet spheres denote Zr and Bi ions, respectively. The S (I) atoms in the top and bottom layers of ZrS₂ (BiI₃) are represented with yellow (blue) and golden (green) spheres, respectively (Color figure online).

cell of BiI₃. The mismatch between the two is about 2%, with the ZrS₂ layer slightly smaller than BiI₃. Hence, when the HS is to be constructed with the lattice parameter of BiI₃, the ZrS₂ layer experience a tensile strain. Similarly, when the HS is constructed with the ZrS₂ lattice parameter, the BiI₃ layer experiences a compressive strain. To minimize this strain due to the lattice mismatch, we further optimized the lattice parameter of the HS. Moreover, depending on the way the two MLs are stacked to form the HS, there are three non-equivalent configurations. To explain the stacking, we label the three sublayers of ML-ZrS₂ by A, B and C and that of ML-BiI₃ by A', B' and C' as displayed in Fig. 2(a). Additionally, we define sulphur (iodine) atoms belonging to sublayers C (C') and A (A') as S_{up} (I_{up}) and S_{down} (I_{down}), respectively. In the B'BC configuration each of the B' atoms (Bi atoms) of BiI₃ is placed on the B and C atoms of ZrS₂, i.e., on the Zr (in sub-layer B) and S_{up} (in sub-layer C) of ML-ZrS₂ as shown by dotted lines in Fig. 2a and b. The B'BA configuration is generated by placing each of the B' atoms of ML-BiI₃ on the B and A atoms of ZrS₂, i.e., on Zr and S_{down} belonging to ML-ZrS₂ (Fig. 2c, d). In the B'AC configuration the two B' atoms (Bi) of ML-BiI₃ are placed on the A and C atoms (S_{down} belonging to A sublayer and S_{up} belonging to C sublayer, respectively) of ML-ZrS₂ as depicted in Fig. 2e, f.

In order to compare the thermodynamic stability of the HS and to determine the lowest energy configuration we have computed the binding energy (E_{BE}) of the heterostructure. E_{BE} is given by:

$$E_{BE} = \frac{E_{HS} - E_{BiI_3} - E_{ZrS_2}}{A}, \quad (4)$$

where E_{HS} , E_{BiI_3} and E_{ZrS_2} are the total energies of the HS, BiI₃, and ZrS₂, respectively. A denotes the

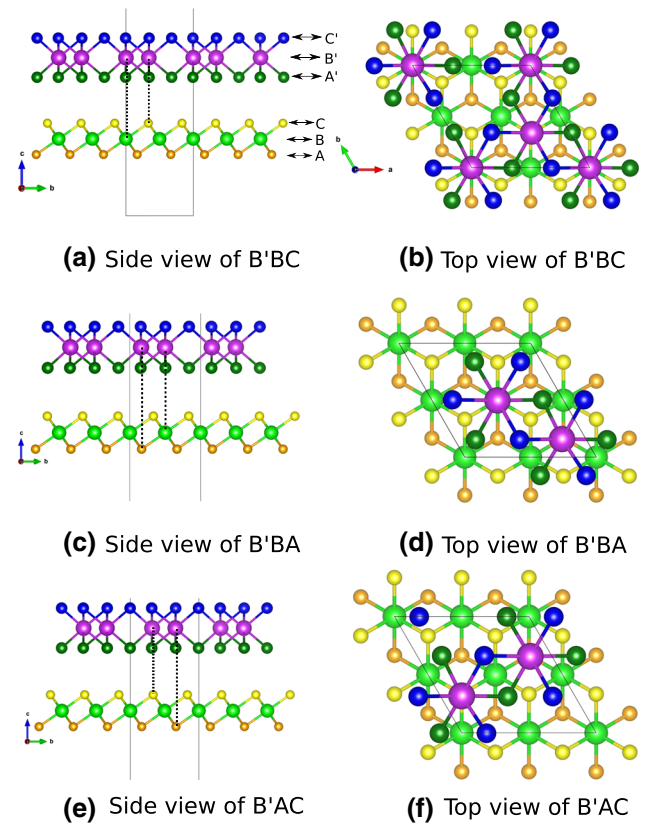


Fig. 2. The side (a, c and e) and top view (b, d and f) for HS-BiI₃/ZrS₂ in configurations (B'BC, B'BA and B'AC, respectively). The Bi, Zr, I_{up} , I_{down} , S_{up} and S_{down} atoms are represented by violet, light green, blue, dark green, yellow and golden colored spheres, respectively (Color figure online).

area of the HS unit cell. The binding energy and the optimized lattice parameter for each of the three configurations are listed in Table II. We find that all three configurations of the HS have the same lattice parameter, 7.30 Å. The B'BC configuration is lowest

in energy with a binding energy of $-0.165 \text{ J}/\text{\AA}^2$. We note that the B'AC and B'BA are about 18 and 2 meV higher in energy than that of the B'BC configuration. Similar values of the binding energy were also observed in HS of graphene and BiI_3 .⁴⁰

The separation between the two layers in the HS is about 3.46 \AA . Similar separation is also observed in other HS, e.g. between graphene/ BiI_3 , MX_2/MX_2 ($M=\text{Zr},\text{Hf}$ and $X=\text{S},\text{Se}$) and transition metal dichalcogenides.^{40–42} The thickness of the ZrS_2 and BiI_3 in the HS are 2.94 \AA and 3.76 \AA , respectively. While the thickness of ZrS_2 in the HS remain unchanged compared to that observed in the monolayer, for BiI_3 it increases by 0.14 \AA up on the formation of the HS. This increase in thickness of the BiI_3 layer in the heterostructure can be attributed to the in-plane compressive strain the BiI_3 layer experiences due to the formation of the HS (lattice parameter of the HS is 7.30 \AA while that of the BiI_3 monolayer is 7.41 \AA). The Bi-I bond length in the heterostructure is about 3.10 \AA and is similar to that observed in the BiI_3 monolayer.

Table II. The lattice parameters (a) and binding energy per unit area (E_{BE}) of the three possible configurations of the HS- $\text{BiI}_3/\text{ZrS}_2$ obtained with PBE+vdW+SOC

Configuration	a (\AA)	E_{BE} ($\text{J}/\text{\AA}^2$)
B'BC	7.30	- 0.165
B'AC	7.30	- 0.164
B'BA	7.30	- 0.159

Within the ZrS_2 layer in the heterostructure, the Zr-S bond lengths are similar to that observed in the ZrS_2 monolayer.

Electronic Properties

As mentioned in the previous section, all three configurations of the HS are similar in energy. Hence, for the study of the electronic and transport properties we used the B'BC configuration.

Figure 3 shows the band structures of ZrS_2 , BiI_3 and HS calculated with PBE (blue lines) and GAU-PBE (red lines) functionals. For both the functionals we used vdW corrections and incorporated SOC interactions. The monolayers have indirect band gaps as seen in Fig. 3a and b. ZrS_2 has a band gap of 1.00 eV at the PBE level, with the valence band maxima (VBM) at the Γ point of the BZ and the conduction band minima at the M -point (Fig. 3b). In contrast, BiI_3 has a band gap that is about 0.36 eV larger than that of ZrS_2 . For the former, the VBM lies along the $\Gamma \rightarrow M$ direction of the BZ while the CBM is at the Γ point (Fig. 3b). Additionally, we find another maxima that are very close in energy to the VBM along the $\Gamma \rightarrow K$ direction. Moreover, as mentioned in the introduction, the valence band edge exhibits a Mexican-hat like structure in the dispersion of VBM around the Γ -point of the BZ. We note that similar band dispersion resulted in high values of Seebeck coefficient for holes in other materials.⁴³ The major effect of the hybrid functional is the shift in the positions of the CBM and VBM that results in an increase in the band gap. However, we observe a larger increase in the band gap for ZrS_2 compared to BiI_3 . For example, while

Table III. The band gap (E_g , in eV) of BiI_3 , ZrS_2 and the B'BC configuration of the HS obtained with PBE and Gau-PBE hybrid functionals

Systems	E_g (ours, PBE)	E_g (ours, Gau-PBE)	E_g (others, PBE)	E_g (others, HSE)	E_g (others, GW)
ML- ZrS_2	1.01	1.91	1.02, ⁴⁴ 1.10 ¹⁸	2.16 ⁴⁴	1.95 ⁴⁵
ML- BiI_3	1.43	1.64	1.55, ²² 1.57 ⁴⁰	2.21 ²²	–
HS- $\text{BiI}_3/\text{ZrS}_2$	0.72	1.20	–	–	–

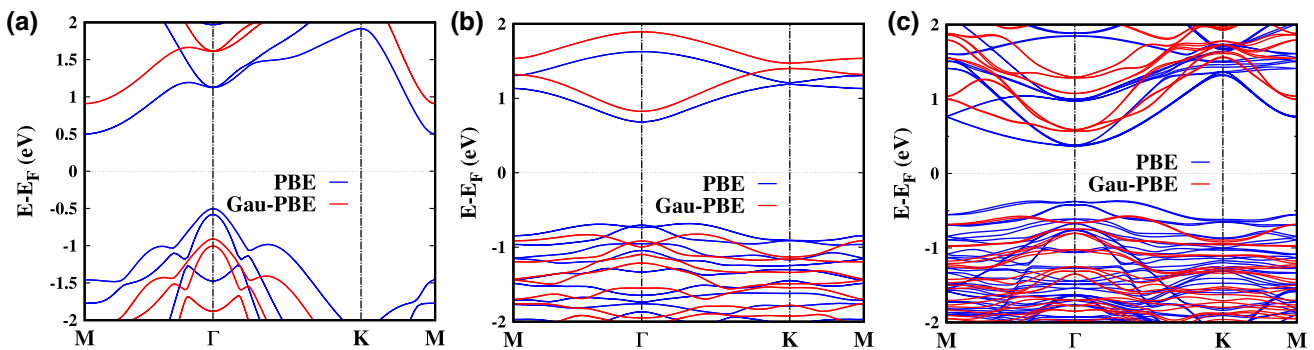


Fig. 3. The electronic band structure computed using PBE (blue) and Gau-PBE (red) functionals for monolayers of ZrS_2 (a), BiI_3 (b) and the B'BC configuration of the HS(c). The Fermi energy is set to zero (Color figure online).

for BiI₃ the band gap increases to 1.64 eV with Gau-PBE functional (0.28 eV increase), the band gap for ZrS₂ also increases to 1.91 eV (about 0.9 eV increase). This can be attributed to the fact that both the valence and conduction bands of ZrS₂ are more shifted compared to that of BiI₃. Unlike BiI₃, where the VBM and CBM are shifted by about 0.14 eV each, for ZrS₂ we observe a shift of 0.41 eV each for the VBM and CBM. The band dispersion is more or less similar to that obtained with PBE (red curves in Fig. 3).

We compared our computed values of the band gaps of the monolayers with those reported in literature (PBE, HSE-functional and GW calculations) in Table III. For the ZrS₂, our PBE results are in excellent agreement with the corresponding ones in the literature.^{18,44} While in the literature, most studies used the HSE functionals, we used Gau-PBE functionals. We find that the values of the band-gap obtained from our Gau-PBE calculations

is about 0.25 eV smaller than those obtained with HSE.⁴⁴ However, our band gap is in excellent agreement with those obtained using more accurate GW calculations.⁴⁵ For BiI₃, we find that our PBE band gaps are slightly smaller than those reported in the literature.^{22,40} This is because in those studies vdW interactions have not been taken into account.

Upon the formation of the HS, we find that the VBM of the HS is localized on BiI₃ and the CBM is localized on ZrS₂ (Fig. 3). This is further corroborated by the plot of the band structure showing contributions from ZrS₂ and BiI₃ in Fig. 4a. Although the band dispersions of the conduction and valence band looks very similar to those of ZrS₂ and BiI₃ monolayers, respectively, a closer look at the band structure shows subtle differences, which, as discussed in the next section, can affect the transport properties of the HS. Figure 5a shows the dispersion of the conduction band edge of the HS

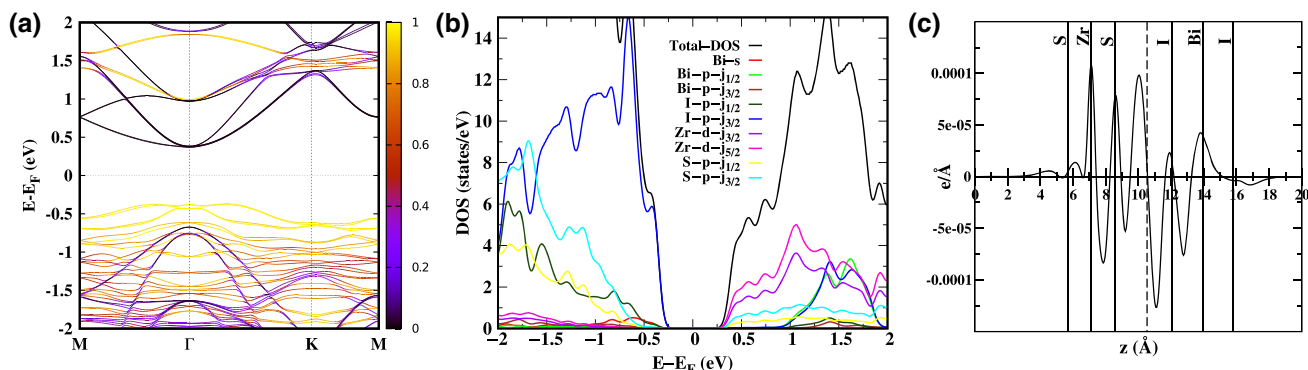


Fig. 4. (a) The band structure of the HS projected on the BiI₃ electronic states. Black lines represent the bands arising from ZrS₂ and colored lines represent the bands arising from BiI₃. (b) The density of states projected onto the atomic orbitals of Bi, Zr, I and S. Both are computed using PBE+vdW+SOC. (c) Planar average of the charge transfer due to the formation of the HS (Color figure online).

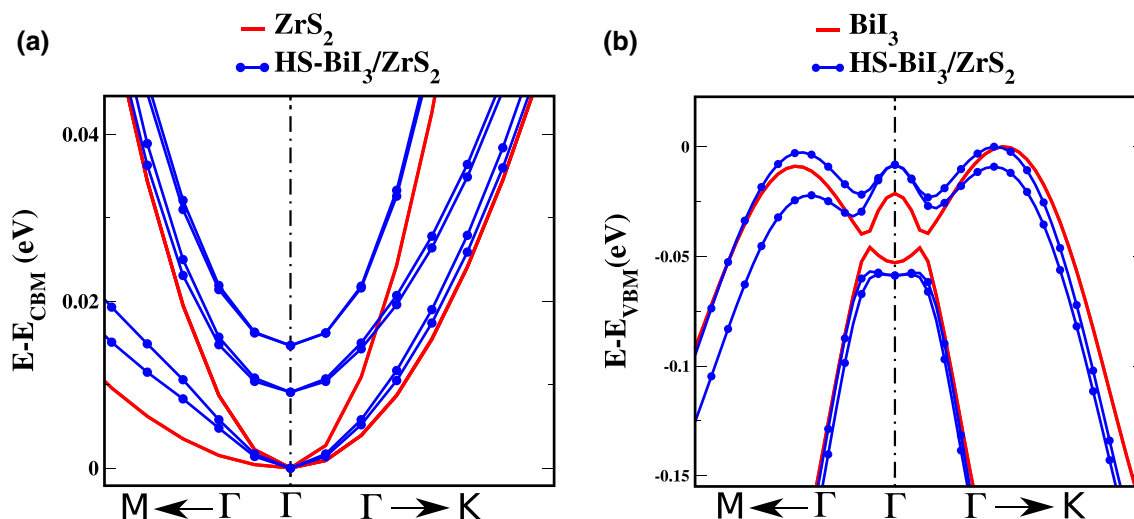


Fig. 5. Magnified view of the band structure around (a) the conduction band minima and (b) valence band maxima of the HS. For sake of comparison, also shown in (a) and (b) the same for ZrS₂ and BiI₃ monolayers, respectively. For both cases, the bands are shifted with respect to the minima and maxima, respectively (Color figure online).

and ZrS₂ monolayer around the Γ -point. For ZrS₂ monolayer, there are six degenerate bands at the Γ point. On moving away from the CBM, they split into a set of two bands, the flatter one has a pair of degenerate bands while the second one has 4 bands. In contrast, in the heterostructure, the bands split weakly resulting into three sets of bands at the Γ point. Each of these have two degenerate bands. Additionally, we observe that the curvature of the bands also increases in the HS, compared with that in ZrS₂ monolayer. On comparing the valence band edge of the HS with that of BiI₃ monolayer (Fig. 5b), we find that the two almost degenerate maxima around the Γ -point shows slight changes. In the HS, this degeneracy is broken and we observe a maxima along the $\Gamma \rightarrow K$ direction. Further, the Mexican-hat like dispersion observed in BiI₃ remains intact even in the HS. In contrast with the ZrS₂ ML, we find the CBM of the HS lies at the Γ -point of the BZ. The change in the position of the CBM in the BZ can be attributed to the folding of the BZ in the reciprocal space for the HS. We note that the unit cell of the HS in real (reciprocal) space is twice (half) that of ZrS₂. As a result the M point of the larger BZ of ZrS₂ folds into the Γ -point of the smaller BZ of the HS.

The HS belongs to type-II with a PBE-band gap of about 0.72 eV (1.20 eV with Gau-PBE). Because of the staggered nature of the alignment of the bands of the individual components of the HS, we find that its band gap is significantly reduced compared to the individual monolayers. Additionally, we find that the weak interaction between the two ML results in small amount of charge transfer (Fig. 4c) from BiI₃ to ZrS₂. As a result the occupied BiI₃ states of move closer to the Fermi level. Further, the density of states (DOS) projected onto the atomic orbitals (Fig. 4b) show that the VBM of the heterostructures have states comprising primarily from I- p orbitals while the CBM have major contributions from Zr- d orbitals.

Computation of Relaxation Time

Table IV lists the values of C , m^* , E_{dp} and τ for the three systems. Since C and E_{dp} are related to the acoustic phonons, we note that the computation of τ by the above mentioned method ignores the contributions coming from coupling of optical

phonons with the electrons. Amongst the three systems, we find that BiI₃ has the lowest value of C while the HS has the largest. The same for ZrS₂ lies at an intermediate value. The larger value of C for the HS compared to that of the individual monolayers can be attributed to the strain in the monolayers due to formation of the HS and the van der Waals interaction between them. We note that similar enhanced strain was also observed in heterostructures of MoS₂/WS₂⁴⁶ and graphene/MoS₂.⁴⁷ Further, the negative sign of E_{dp} for both the valence and conduction band implies that upon deformation, both the band edges go down in energy. The magnitude of E_{dp} is an indication of the strength of electron-phonon coupling in these systems. A comparison of $|E_{dp}|$ between the holes and electrons suggests that holes couple more strongly with the lattice vibrations compared to electrons. In the heterostructure, the $|E_{dp}|$ for electrons (holes) are similar to that of ZrS₂ (BiI₃).

The effective masses show significant amount of anisotropy based on transport direction. While for BiI₃, m^* for electrons has the largest value along the zigzag direction, for ZrS₂ it is heaviest along the armchair direction. In BiI₃ the holes are heaviest along the armchair direction. In contrast, in ZrS₂, along both the directions, the holes have a lighter mass. For the HS, it is expected that the effective masses of electrons (holes) will be similar to that of ZrS₂ (BiI₃). From Table IV we find that the effective mass of electrons along the zigzag direction is indeed similar to that of ZrS₂. However, along the armchair direction we find that the electron effective mass is significantly reduced compared to that in ZrS₂ along the same direction. This can be attributed to the changes in the band dispersion observed in the conduction band of the HS due to the interactions between ZrS₂ and BiI₃. For the holes, as per our expectation, we find that the effective masses are close to that observed in BiI₃.

The combined effect of C , m^* , E_{dp} results in smallest value of relaxation time in BiI₃ for both electrons and holes. Amongst the three systems, the electrons in the HS have the largest value of τ . This is primarily because of the reduction of the effective masses of electrons in the HS along the armchair direction. For holes largest value of τ is observed in

Table IV. C , m^* , E_{dp} and τ for the electrons and holes in ZrS₂ and BiI₃ monolayers and in the HS

System		C (eV/Å ²)	m^* (zigzag) (m_e)	m^* (armchair) (m_e)	E_{dp} eV	τ (10 ⁻¹⁴ s)		
						$T = 300$ K	$T = 400$ K	$T = 500$ K
ZrS ₂	Electron	6.04	0.28	1.97	- 3.41	1.87	1.40	1.12
	Hole							
BiI ₃	Electron	1.29	2.06	0.50	- 5.14	0.93	0.70	0.56
	Hole							
HS	Electron	7.42	0.29	0.56	- 3.81	24.60	18.50	14.80
	Hole							

ZrS₂ monolayer. Further, the relaxation time decreases with increase in temperature.

Electronic Transport Properties

Based on the electronic structure of the three materials we now evaluate the transport coefficients of these three materials by solving the Boltzmann transport equations. Figure 6 shows the plots of the Seebeck coefficient (α) as a function of chemical potential. Figure 7 (Fig. 8) shows the plots for electrical conductivity (σ), power factor ($PF/\tau = \alpha^2\sigma$) and (κ_e) for the three systems for holes (electrons). These properties have been computed using the band dispersion obtained from PBE calculations. The PBE band gap has been corrected with the Gau-PBE one for each of the cases.

Near the band edges, we observe that the maximum values of α is similar for all three cases varying between 1.81 and 3.15 mV/K for holes and electrons at 300 K (Fig. 7a–c). With other factors remaining

constant, it is usually expected that a larger band gap results in a greater value of Seebeck coefficient at the band edges. This is because the magnitude of S for non-degenerate semiconductors depends on the distance between the energy at which S is computed and the Fermi level (E_F), the latter is typically close to the middle of the band gap. We note that though ZrS₂ has a larger band gap than BiI₃ and the HS, we find that the Seebeck coefficients for the three systems are comparable. This can be attributed to the fact that even though the latter two have a smaller band gaps than ZrS₂, they have a Mexican-hat like structure at the valence band edge, that gives rise to three almost degenerate maxima. In contrast, for ZrS₂, there is just one maximum. This results in increase of density of states at the valence band edge for BiI₃ and the HS, that inturn increases the value of α . Moreover, compared with that of the monolayers, for the HS the Seebeck coefficient decreases more rapidly with

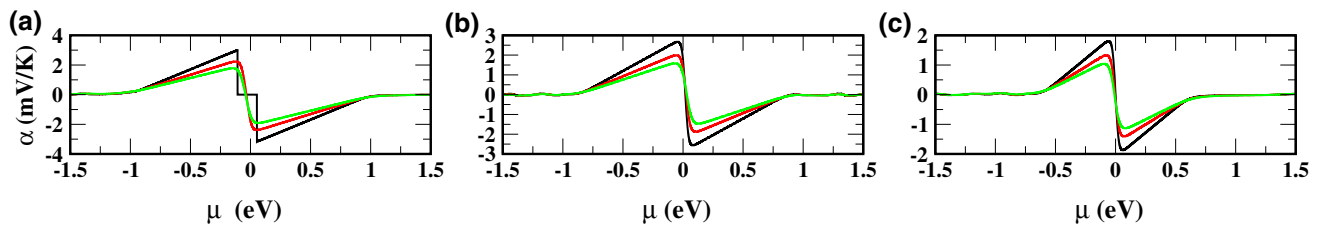


Fig. 6. Seebeck coefficient (α) as a function of chemical potential (μ) in (a) ZrS₂, (b) BiI₃ and (c) HS. The black, red and green plots are at 300, 400 and 500 K, respectively. Negative (positive) values of μ denote holes (electrons) (Color figure online).

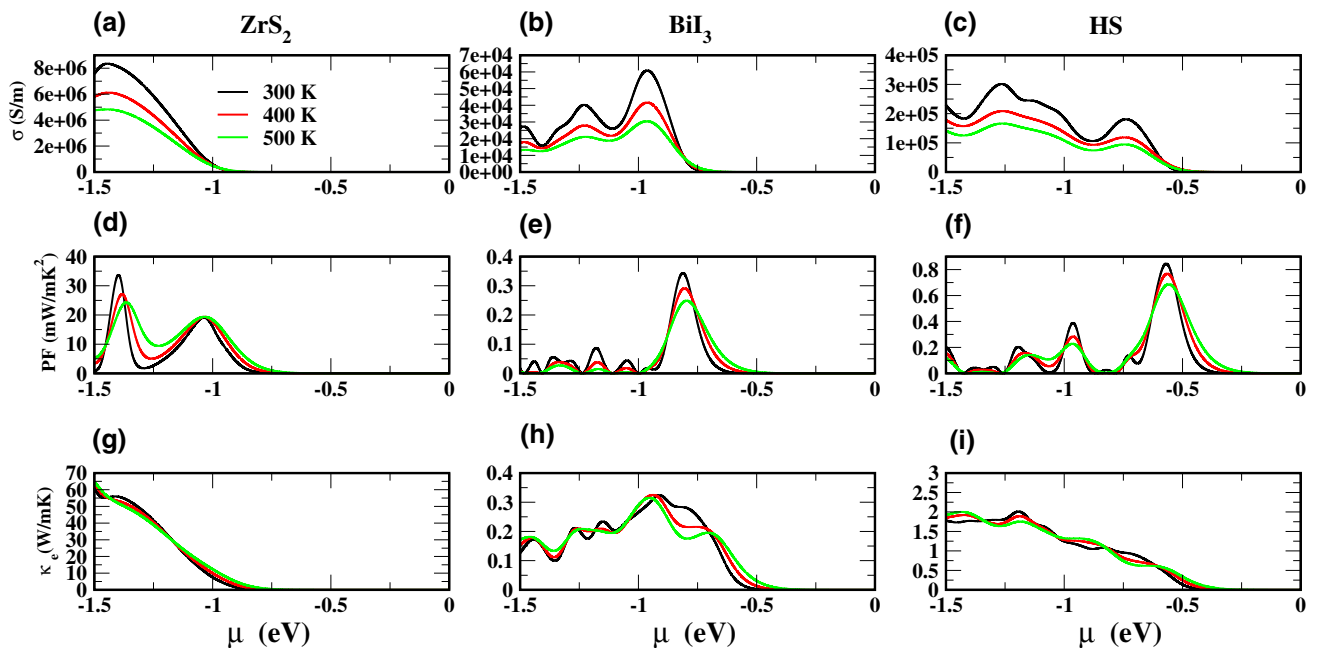


Fig. 7. Electronic conductivity, σ (a, b, c), power factor PF (d, e, f) and electronic contribution to thermal conductivity, κ_e (g, h, i) for holes as a function of the chemical potential (μ) at three different temperatures, namely 300 K, 400 K and 500 K. The first, second and third columns are results for ZrS₂, BiI₃ and the HS, respectively (Color figure online).

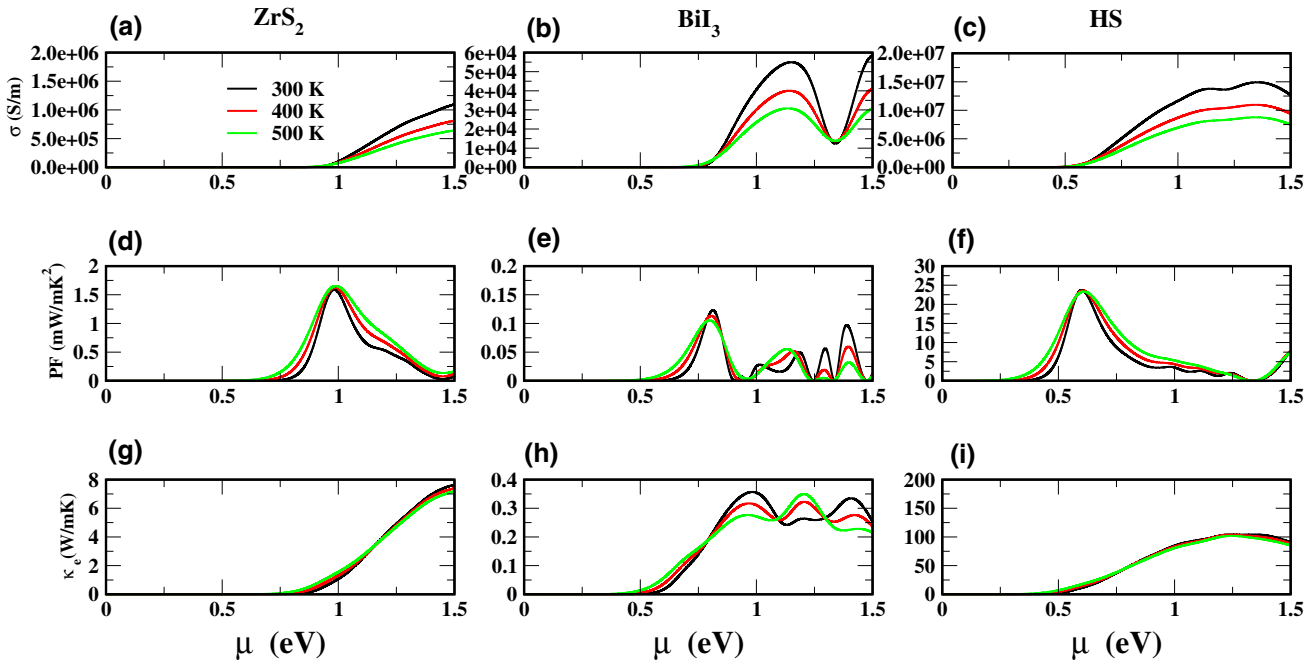


Fig. 8. Electronic conductivity, σ (a, b, c), power factor PF (d, e, f) and electronic contribution to thermal conductivity, κ (g, h, i) for electrons as a function of the chemical potential (μ) at three different temperatures, namely 300 K, 400 K and 500 K. The first, second and third columns are results for ZrS₂, BiI₃ and the HS, respectively (Color figure online).

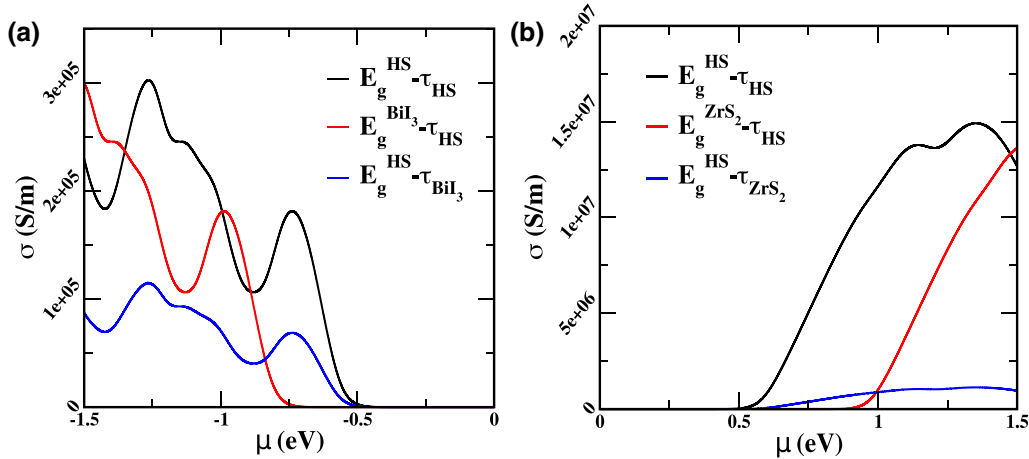


Fig. 9. Effect of τ and band gap on σ of holes (a) and electrons (b). In the figure legend, E_g denotes band gap and τ denotes the relaxation time (Color figure online).

higher value of chemical potential, i.e. increase in carrier concentration. On increasing the temperature, we find that there is a reduction of the Seebeck coefficient for all the cases.

Compared to BiI₃, the σ values for ZrS₂ are larger for both electrons and holes (Figs. 7a, b and 8a, b). However, due to the larger band gap of ZrS₂, we observe that the peaks in the σ plots occur at higher value of chemical potential. This implies that larger number of charge carriers are necessary to achieve electrical conductivity in ZrS₂ than in BiI₃. For example, while in BiI₃, the first peak in σ for holes is at $\mu = -0.96$ eV (9.88×10^{14} cm⁻² carrier concentration), for ZrS₂ the same occurs at 1.54 eV,

corresponding to a carrier concentration of 1.69×10^{15} cm⁻². The holes in the HS resides in BiI₃ and since the dispersion of the valence band is similar in both the cases, one would have expected that the σ values for the holes in HS should be closer to that observed in BiI₃. However, we observe that in HS σ is one order of magnitude larger than that in BiI₃ (Fig. 7b and c). This can be attributed to the faster relaxation times of holes in the HS. Amongst the three materials considered in this study, for holes, it is observed that ZrS₂ shows largest value of σ (Fig. 7a). For the electrons, amongst the three systems, the HS shows the largest value of σ . In fact σ of electrons in the HS is one order of magnitude

larger than that observed in ZrS₂ and three orders of magnitude larger than that observed in BiI₃ (Fig. 8a–c). Since the band gap of the HS is significantly smaller than that of the individual monolayers, we observe the peaks in conductivity at a lower value of the chemical potential. For example, for holes, the first peak is at -0.74 eV, corresponding to a chemical potential of 2.86×10^{14} cm⁻² while for electrons, the first peak is observed at 1.14 eV corresponding to a carrier concentration of 6.71×10^{14} cm⁻².

Further, to separate out the effects of the band gap and τ on the conductivity of the charge carriers in the HS, in Fig. 9 we plotted σ of the HS as a function of the chemical potential using the band gaps and τ of the individual components of the HS. Since the holes reside in BiI₃, we have computed σ for HS with band gap of BiI₃ and τ_{HS} and also with band gap of HS and τ_{BiI_3} (Fig. 9a). Similarly for electrons, we used the band gap and τ of ZrS₂ (Fig. 9b). A comparison of the σ plot computed with the band gap of the HS and τ_{HS} (black line in Fig. 9a) with that calculated with the band gap of BiI₃ and τ_{HS} (red line in Fig. 9a) shows that the primary effect of the reduced band gap of the HS is that it changes the doping concentration at which one can observe a given value of conductivity. The plot with a larger band gap shifts to higher (in magnitude) value of μ . In contrast, when we compare the σ computed with the band gap and τ of the HS (black line in Fig. 9a) with that calculated with the band gap of HS and τ_{BiI_3} (blue line in Fig. 9a) we observe that the magnitude of σ changes because the τ are different in the two cases. Similar effect is also observed for electrons (Fig. 9b). However, for electrons the effect of τ is larger because the magnitude of τ for electrons in HS is about 13 times larger than that observed in ZrS₂.

The power factor is a good measure of a thermoelectric performance of a device. Figures 7d–f and 8d–f shows the variation of PF with μ for the three cases. Analogous to the conductivity plots, we find that for the monolayers, the PF for both the electrons and holes are larger in ZrS₂ than in BiI₃. In ZrS₂ the PF for the holes are larger than that observed for electrons, while in BiI₃ they are comparable. For the HS, the PF values of the electrons are not only larger than that of the holes, but also they are largest compared to the individual monolayers. This suggests that the heterostructure might show an improved performance over its individual monolayers as a n -type thermoelectric. Further, in comparison with the monolayers, we can achieve a large value of PF at lower carrier concentration. For example, for holes, the first peak in PF observed in ZrS₂ and BiI₃ corresponds to 1.25×10^{15} cm⁻² and 4.72×10^{14} cm⁻² holes, respectively, while in the HS, values of PF similar to that of BiI₃ can be observed at 3.75×10^{13} cm⁻² holes. The corresponding numbers for electrons are

4.41×10^{14} cm⁻² and 2.36×10^{14} cm⁻² for ZrS₂ and BiI₃, respectively, compared with 2.81×10^{13} cm⁻² for the HS. In addition to the PF , we have computed the electronic contribution to the thermal conductivity (κ_e) for the three cases (Fig. 7g–i for holes and Fig. 8g–i for electrons). For all three cases, the behaviour is similar to that observed for σ .

CONCLUSION

In conclusion, we have investigated the electronic and transport properties of monolayers of ZrS₂ and BiI₃ and a vertical HS formed using them for plausible application for thermoelectric devices. While the individual materials have a large band gap, the HS forms a type II junction with a reduced band gap of 1.20 eV. This reduction in band gap results in significant amount of electrical conductivity and PF at low concentration of electrons and holes. Further, the interactions between the monolayers in the HS induce subtle changes in the band dispersion such that electron effective masses are significantly different in the HS than in ZrS₂ monolayer. Moreover, from the calculation of deformation potential and two-dimensional elastic constants, we find that the phonons of the HS are hardened compared to that of the individual monolayer. All these changes in the electronic and structural properties of the HS results in significantly different relaxation times of charge carriers in the HS compared to that of ZrS₂ or BiI₃. Further, these are also reflected in their transport properties. In particular, we find that for the electrons in the HS, the power factor is 10 and 100 times larger than those observed in ZrS₂ and BiI₃. This suggests that the maximum power output from a device made with n -doped heterostructure will be larger than that of the individual components. This suggest that the HS is a plausible candidate for an n -type thermoelectric. However, we note that the efficiency of the device needs to be tested by computing ZT , computation of which is beyond the scope of the present study. We hope that our results will motivate further experimental and theoretical studies on this HS.

ACKNOWLEDGMENTS

The authors acknowledge CDAC-Pune, Centre for Modeling and Simulations, Pune University and Param-Brahma for computational resources. Gautam Sharma would like to thank IISER-Pune for the fellowship.

CONFLICT OF INTEREST

The authors declare that they have no conflict of interest.

REFERENCES

1. F.J. DiSalvo, *Science* 285(5428), 703 (1999). <https://doi.org/10.1126/science.285.5428.703>.

2. L.E. Bell, *Science* 321(5895), 1457 (2008). <https://doi.org/10.1126/science.1158899>.
3. C. Han, Z. Li, and S. Dou, *Chin. Sci. Bull.* 59(18), 2073 (2014). <https://doi.org/10.1007/s11434-014-0237-2>.
4. L.D. Hicks, and M.S. Dresselhaus, *Phys. Rev. B* 47, 12727 (1993). <https://doi.org/10.1103/PhysRevB.47.12727>.
5. L.D. Hicks, and M.S. Dresselhaus, *Phys. Rev. B* 47, 16631 (1993). <https://doi.org/10.1103/PhysRevB.47.16631>.
6. V. Goyal, D. Teweldebrhan, and A.A. Balandin, *Appl. Phys. Lett.* 97(13), 133117 (2010). <https://doi.org/10.1063/1.3494529>.
7. T.C. Harman, P.J. Taylor, M.P. Walsh, and B.E. LaForge, *Science* 297(5590), 2229 (2002). <https://doi.org/10.1126/science.1072886>.
8. T.C. Harman, M.P. Walsh, B.E. Laforge, and G.W. Turner, *J. Electron. Mater.* 34(5), L19 (2005). <https://doi.org/10.1007/s11664-005-0083-8>.
9. J. Mao, Z. Liu, and Z. Ren, *Npj Quantum Mater.* 1, 1 (2016). <https://doi.org/10.1038/npjquantmats.2016.28>.
10. L. Cheng, H. Liu, X. Tan, J. Zhang, J. Wei, H. Lv, J. Shi, and X. Tang, *J. Phys. Chem. C* 118(2), 904 (2014). <https://doi.org/10.1021/jp411383j>.
11. K.X. Chen, X.M. Wang, D.C. Mo, and S.S. Lyu, *J. Phys. Chem. C* 119(47), 26706 (2015). <https://doi.org/10.1021/acs.jpcc.5b06728>.
12. J.R. Sootsman, H. Kong, C. Uher, J.J. D'Angelo, C.I. Wu, T.P. Hogan, T. Caillat, and M.G. Kanatzidis, *Angew. Chem. Int. Edit.* 47(45), 8618 (2008). <https://doi.org/10.1002/anie.200803934>.
13. Z. Liu, J.O. Morales-Ferreiro, and T. Luo, *Appl. Phys. Lett.* 113(6), 063903 (2018). <https://doi.org/10.1063/1.5040888>.
14. H. Babaei, J.M. Khodadadi, and S. Sinha, *Appl. Phys. Lett.* 105(19), 193901 (2014). <https://doi.org/10.1063/1.4901342>.
15. W. Huang, H. Da, and G. Liang, *J. Appl. Phys.* 113(10), 104304 (2013). <https://doi.org/10.1063/1.4794363>.
16. D. Wickramaratne, F. Zahid, and R.K. Lake, *J. Chem. Phys.* 140(12), 124710 (2014). <https://doi.org/10.1063/1.4869142>.
17. M. Buscema, M. Barkelid, V. Zwiller, H.S.J. van der Zant, G.A. Steele, and A. Castellanos-Gomez, *Nano Lett.* 13(2), 358 (2013). <https://doi.org/10.1021/nl303321g>. PMID: 23301811.
18. H.Y. Lv, W.J. Lu, D.F. Shao, H.Y. Lu, and Y.P. Sun, *J. Mater. Chem. C* 4, 4538 (2016). <https://doi.org/10.1039/C6TC01135G>.
19. J. Liu, Q. Sun, Y. Kawazoe, and P. Jena, *Phys. Chem. Chem. Phys.* 18, 8777 (2016). <https://doi.org/10.1039/C5CP04835D>.
20. C. Huang, J. Zhou, H. Wu, K. Deng, P. Jena, and E. Kan, *Phys. Rev. B* 95, 045113 (2017). <https://doi.org/10.1103/PhysRevB.95.045113>.
21. J. He, S. Ma, P. Lyu, and P. Nachtigall, *J. Mater. Chem. C* 4, 2518 (2016). <https://doi.org/10.1039/C6TC00409A>.
22. W.B. Zhang, L.J. Xiang, and H.B. Li, *J. Mater. Chem. A* 4, 19086 (2016). <https://doi.org/10.1039/C6TA06806E>.
23. P. Liu, F. Lu, M. Wu, X. Luo, Y. Cheng, X.W. Wang, W. Wang, W.H. Wang, H. Liu, and K. Cho, *J. Mater. Chem. C* 5, 9066 (2017). <https://doi.org/10.1039/C7TC03003G>.
24. D. Wickramaratne, F. Zahid, and R.K. Lake, *J. Appl. Phys.* 118(7), 075101 (2015). <https://doi.org/10.1063/1.4928559>.
25. P. Gorai, E.S. Toberer, and V. Stevanović, *J. Mater. Chem. A* 4, 11110 (2016). <https://doi.org/10.1039/C6TA04121C>.
26. M.K. Mohanta, A. Rawat, N. Jena, Dimple, R. Ahammed, and A. De Sarkar, *ACS Applied Materials & Interfaces* 12(2), 3114 (2020). <https://doi.org/10.1021/acsami.9b16866>. PMID: 31904214.
27. V.H. Nguyen, M.C. Nguyen, H.V. Nguyen, J. Saint-Martin, P. Dollfus, *Appl. Phys. Lett.* 105(133), 133105 (2014). <http://doi.org/10.1063/1.4896915>.
28. G. Ding, C. Wang, G. Gao, K. Yao, C. Dun, C. Feng, D. Li, and G. Zhang, *Nanoscale* 10, 7077 (2018). <https://doi.org/10.1039/C7NR09029C>.
29. P. Giannozzi, S. Baroni, N. Bonini, M. Calandra, R. Car, C. Cavazzoni, D. Ceresoli, G.L. Chiarotti, M. Cococcioni, I. Dabo, A. Dal Corso, S. de Gironcoli, S. Fabris, G. Fratesi, R. Gebauer, U. Gerstmann, C. Gougoussis, A. Kokalj, M. Lazzeri, L. Martin-Samos, N. Marzari, F. Mauri, R. Mazzarello, S. Paolini, A. Pasquarello, L. Paulatto, C. Sbraccia, S. Scandolo, G. Sclauzero, A.P. Seitsonen, A. Smogunov, P. Umari, and R.M. Wentzcovitch, *J. Phys. Condensed Matter*. 21(39), 395502 (2009).
30. P. Giannozzi, O. Andreussi, T. Brumme, O. Bunau, M.B. Nardelli, M. Calandra, R. Car, C. Cavazzoni, D. Ceresoli, M. Cococcioni, N. Colonna, I. Carnimeo, A.D. Corso, S. de Gironcoli, P. Delugas, R.A.D.A. Ferretti Jr., A. Floris, G. Fratesi, G. Fugallo, R. Gebauer, U. Gerstmann, F. Giustino, T. Gorni, J. Jia, M. Kawamura, H.Y. Ko, A. Kokalj, E. Küçükbenli, M. Lazzeri, M. Marsili, N. Marzari, F. Mauri, N.L. Nguyen, H.V. Nguyen, A.O. de-la Roza, L. Paulatto, S. Poncé, D. Rocca, R. Sabatini, B. Santra, M. Schlipf, A.P. Seitsonen, A. Smogunov, I. Timrov, T. Thonhauser, P. Umari, N. Vast, X. Wu, and S. Baroni, *J. Phys. Condensed Matter*. 29(46), 465901 (2017).
31. J.P. Perdew, K. Burke, and M. Ernzerhof, *Phys. Rev. Lett.* 77, 3865 (1996). <https://doi.org/10.1103/PhysRevLett.77.3865>.
32. D. Vanderbilt, *Phys. Rev. B* 41, 7892 (1990).
33. H.J. Monkhorst, and J.D. Pack, *Phys. Rev. B* 13, 5188 (1976). <https://doi.org/10.1103/PhysRevB.13.5188>.
34. G. Stefan, *J. Comput. Chem.* 27(15), 1787 (2006). <https://doi.org/10.1002/jcc.20495>.
35. A. Dal Corso, *Comput. Mater. Sci.* 95, 337 (2014). <https://doi.org/10.1016/j.commatsci.2014.07.043>.
36. A.D. Corso, and A.M. Conte, *Phys. Rev. B* 71, 115106 (2005). <https://doi.org/10.1103/PhysRevB.71.115106>.
37. J.W. Song, G. Giorgi, K. Yamashita, and K. Hirao, *J. Chem. Phys.* 138(24), 241101 (2013). <https://doi.org/10.1063/1.4811775>.
38. D.R. Hamann, M. Schlüter, and C. Chiang, *Phys. Rev. Lett.* 43, 1494 (1979). <https://doi.org/10.1103/PhysRevLett.43.1494>.
39. G.K. Madsen, and D.J. Singh, *Comput. Phys. Commun.* 175(1), 67 (2006). <https://doi.org/10.1016/j.cpc.2006.03.007>.
40. M. Fengxian, Z. Mei, J. Yalong, G. Guoping, G. Yuantong, B. Ante, C. Zhongfang, and D. Aijun, *Sci. Rep.* 5, 1 (2015). <https://doi.org/10.1038/srep17558>.
41. F. Khan, H. Din, S. Khan, G. Rehman, M. Bilal, C.V. Nguyen, I. Ahmad, L.Y. Gan, and B. Amin, *J. Phys. Chem. Solids* 126, 304 (2019). <https://doi.org/10.1016/j.jpics.2018.11.021>.
42. B. Amin, N. Singh, and U. Schwingenschlögl, *Phys. Rev. B* 92, 075439 (2015). <https://doi.org/10.1103/PhysRevB.92.075439>.
43. X.J. Ge, D. Qin, K.L. Yao, and J.T. Lü, *J. Phys. D Appl. Phys.* 50(40), 405301 (2017).
44. Q. Zhao, Y. Guo, K. Si, Z. Ren, J. Bai, and X. Xu, *Physica Status Solidi (b)* 254(9), 1700033 (2017). <https://doi.org/10.1002/pssb.201700033>.
45. M. Abdulsalam, and D.P. Joubert, *Physica Status Solidi (b)* 253(4), 705 (2016). <https://doi.org/10.1002/pssb.201552584>.
46. K. Liu, Q. Yan, M. Chen, W. Fan, Y. Sun, J. Suh, D. Fu, S. Lee, J. Zhou, S. Tongay, J. Ji, J.B. Neaton, and J. Wu, *Nano Lett.* 14(9), 5097 (2014). <https://doi.org/10.1021/nl501793a>. PMID: 25120033.
47. S. Singh, C. Espejo, and A.H. Romero, *Phys. Rev. B* 98, 155309 (2018). <https://doi.org/10.1103/PhysRevB.98.155309>.

Publisher's Note Springer Nature remains neutral with regard to jurisdictional claims in published maps and institutional affiliations.